Detection of defect populations in superhard semiconductor boron subphosphide $B_{12}P_2$ through x-ray absorption spectroscopy

S. P. Huber,[1,2,*] E. Gullikson,[3] J. Meyer-Ilse,[3] C. D. Frye,[4]
J. H. Edgar,[4] R. W. E. van de Kruijs,[2] F. Bijkerk,[2] and D. Prendergast[1]

[1] *Molecular Foundry, Lawrence Berkeley National Laboratory, Berkeley, California 94720, United States*
[2] *Industrial Focus Group XUV Optics, MESA+ Research Institute for Nanotechnology, University of Twente, P.O. Box 217, 7500 AE, Enschede, The Netherlands*
[3] *Center for X-Ray Optics, Lawrence Berkeley National Laboratory, Berkeley, California 94720, United States*
[4] *Department of Chemical Engineering, Kansas State University, Manhattan, Kansas 66506, United States*

(Dated: Monday 6th March, 2017)

Recent theoretical work[1] has shown for the first time how the experimentally observed property of "self-healing" of the superhard semiconductor boron subphosphide ($B_{12}P_2$) arises through a process of mediated defect recombination. Experimental verification of the proposed mechanism would require a method that can detect and distinguish between the various defect populations that can exist in $B_{12}P_2$. X-ray absorption near-edge spectroscopy (XANES) is such a method and in this work we present experimentally collected spectra of $B_{12}P_2$ samples with varying crystalline qualities. By simulating the x-ray spectroscopic signatures of potential crystallographic point defects from first-principles within the density functional theory framework, the presence of defect populations can be determined through spectroscopic fingerprinting. Our results find an increasing propensity for the presence of phosphorus vacancy defects in samples deposited at lower temperatures but no evidence for comparable populations of boron vacancies in all the samples that have been studied. The absence of large amounts of boron vacancies is in line with the "self-healing" property of $B_{12}P_2$.

I. INTRODUCTION

The boron-rich solid $B_{12}P_2$, also known as boron subphosphide or icosahedral boron phosphide, has been the subject of a variety of research studies, due to its interesting properties including high (radiation) hardness[2], chemical inertness and neutron capture cross-section[3]. The combination of these properties make it an ideal candidate for applications in for example radiation shielding, neutron detectors and betavoltaic cells[3–5]. One of the more intriguing properties of this material, is the alledged observation of a "self-healing" mechanism. Transmission electron microscopy of $B_{12}P_2$ samples, after prolonged exposure to high energy particles, showed no visible damage patterns[6]. Under the conditions of the experiment, in terms of radiation energy and exposure time, it was estimated that each and every boron atom had to have been displaced on the order of 10 times, which, following the lack of observed structural damage, led to the suggestion of an intrinsic "self-healing" property of the material[4,6]. The lack of structural damage was observed in experiments conducted both at room and lowered temperatures of 12 K, suggesting that the mechanism, underlying the restorative quality of $B_{12}P_2$, is active even under conditions of low thermal activity.

In a recent publication[1], the proposed mechanism was investigated theoretically, where the static structural properties of vacancy and interstitial defects and the dynamical process of defect recombination were simulated within the density functional theory (DFT) framework. The calculations revealed that the boron icosahedra, that form the cornerstone of the $B_{12}P_2$ crystal structure, remain structurally stable, even in the presence of a vacancy or interstitial defect. However, for certain configurations of an interstitial and vacancy defect pair (a Frenkel defect), the activation barrier for defect recombination can be almost negligible. This surprisingly low energy barrier would be surmountable even at low temperatures and could potentially explain the experimentally observed "self-healing" in $B_{12}P_2$.

An experimental verification, of the theoretically proposed static defect characteristics and the properties of the dynamic recombination process, is now required. X-ray absorption near-edge spectroscopy (XANES) is sensitive to structural defects in borides[7–11] and could potentially be used to monitor defect formation and defect abundances during sample irradiation. However, to the best of the authors' knowledge, x-ray spectroscopy data for $B_{12}P_2$ has not yet been reported in literature and therefore a reference signature of pristine $B_{12}P_2$ is not available. We will present experimental x-ray absorption spectroscopy measurements of the boron K-edge and phosphorus $L_{2,3}$-edge for several $B_{12}P_2$ samples deposited with chemical vapor deposition under varying conditions.

A theoretical analysis of the collected spectra is conducted from first-principles within the DFT framework, which provides a spectroscopic fingerprint for crystalline $B_{12}P_2$. Additionally, first-principles calculations are employed to simulate the spectroscopic signatures of potential point defects in $B_{12}P_2$, which are used to discuss the abundances of these defects present in the analyzed samples. These defect spectroscopy signatures could be utilized in future studies collecting x-ray absorption spectroscopy measurements of samples during irradiation by high energy particles, to observe the evolution of defect populations *in situ*. The experimental spectroscopic results presented in this work, indicate a lack of boron va-

cancies, in line with the findings of earlier work on the "self-healing" of $B_{12}P_2$, which would predict a lack of boron vacancies by definition.

II. COMPUTATIONAL METHOD

A. Structural relaxations

All structural optimizations have been carried out within the DFT framework using the Vienna *ab initio* simulation package VASP[12]. Core electrons are replaced by ultrasoft pseudopotentials within the projector augmented wave (PAW) method[13,14] where $2s$ and $2p$ electrons for boron and, $3s$ and $3p$ electrons for phosphorus are treated as valence electrons. The generalized gradient approximation (GGA) as formulated by Perdew-Burke-Ernzerhof[15] (PBE) is employed for the exchange-correlation energy. A $2 \times 2 \times 2$ supercell from the $B_{12}P_2$ unitcell was used for all calculations, totalling 336 boron and 48 phosphorus atoms for the perfect crystalline supercell. Plane waves were expanded up to an energy of 400 eV and the Brillouin zone was sampled at the Γ point. In calculations of total energies, for the purpose of computing defect formation energies, the k-point density was increased to a $2 \times 2 \times 1$ Monkhorst-Pack mesh[16], to ensure convergence. In density of states calculations the Brillouin zone integration was performed with the tetrahedron method[17], over a $8 \times 8 \times 4$ Monkhorst-Pack mesh and, where applicable, for screened hybrid functionals the HSE06 functional was employed[18]. Thermally induced structural distortions of the bulk $B_{12}P_2$ crystal lattice were simulated by sampling the canonical ensemble (NVT) at a finite temperature of 300 K regulated by a Nosé-Hoover thermostat. The time step of integration was set to 0.2 fs. The system was thermally equilibrated for 5 ps, after which the sampling was switched to the micro canonical ensemble (NVE) maintaining a temperature of 300 K. From this trajectory three snapshots were taken at intervals of 2.5 ps for which the average x-ray absorption spectrum was calculated, to represent a statistical average of the structure at finite temperature.

B. Formation energies

As an estimate for the likelihood of formation of any of the considered point defects we compute the formation energy E^f, which for a defect X in charge state q is commonly estimated by the equation[19]

$$E^f[X^q] = E[X^q] + E^q_{\text{corr}} - E[\text{host}] - \sum n_i \mu_i + q(\epsilon_F + \epsilon_v + \Delta v), \quad (1)$$

where $E[X^q]$ and $E[\text{host}]$ are the total energies of the defective and pristine host structures, respectively, as derived from supercell calculations. The amount of particles of type i, both native and impure, that are added or removed is given by n_i, which is positive for a net amount of particles added and negative otherwise. Assuming thermodynamic equilibrium, the native and impurity atoms are assumed to be exchanged with a reservoir at a chemical potential given by μ_i which can be related through an equilibrium definition and the chemical potentials of a boron and phosphorus solid phase. In the limit of a boron- or phosphorus rich environment, the corresponding chemical potential can then be computed from the Gibbs free energy from the boron α-rhombohedral or $B_{12}P_2$ bulk phase, respectively, thereby fixing the chemical potential of the other elemental species one through the equilibrium definition. All defect calculations were performed for the neutral charge state and therefore the image-charge correction term E^q_{corr} and the potential alignment term Δv can be ignored[19,20].

C. X-ray absorption spectroscopy

X-ray absorption spectroscopy (XAS) was simulated within the density functional theory excited core-hole (DFT-XCH) approach[21] where the photo excited atom is modeled by removing a core electron from the pseudopotential and placing it in the first available empty state. The electronic structure problem of the system that now includes the core-hole is then solved self-consistently under constrained occupations while employing the Shirley interpolation scheme[22] to generate optimal basis sets in order to reduce computational cost. The absorption spectrum is computed by evaluating the transition probability between the initial and final state as given by Fermi's golden rule within the dipole approximation. The resulting spectrum is broadened uniformly with a Gaussian of 0.2 eV at FWHM. To correct for the well-known underestimation of the band gap by the PBE functional, the energy scale is stretched uniformly by a factor of 1.08 for the boron K-edge and 1.06 for the phosphorus $L_{2,3}$-edge. Due to the lack of an absolute energy reference inherent in the pseudopotential method, an energy alignment scheme was employed to yield comparably meaningful relative energies for structurally and chemically different systems[23]. Finally, the entire spectrum is shifted by a single value, which is kept constant for all computed spectra, to align with the experimental data. In the case of a $L_{2,3}$-edge transition, electrons from either the $2p_{3/2}$ or $2p_{1/2}$ core level can be excited, which, due to spin-orbit coupling, are energetically split. Under the assumption that excitations from $2p_{3/2}$ or $2p_{1/2}$ core levels are equally probable, in this work, this effect is accounted for by adding the spectrum to itself, after shifting it by an energy ΔE equal to the spin-orbit splitting of the relevant element, and properly weighting the two spectra by a ratio of $2:1$ that reflects the population ratio of the $2p_{3/2}$ and $2p_{1/2}$ core levels.

III. EXPERIMENTAL DETAILS

All x-ray absorption spectroscopy measurements were carried out at beamline 6.3.2 of the Advanced Light Source (ALS) synchrotron at Lawrence Berkeley National Laboratory (LBNL). A detailed description and characterization of the beamline and measurement chamber can be found elsewhere[24,25]. X-ray absorption measurements of the boron K-edge and phosphorus $L_{2,3}$ edge, were collected in total electron yield (TEY) mode. The linearly polarized incident soft x-ray beam was oriented parallel to the sample surface normal. Energy calibration was performed by comparing to absolute absorption edges of Si and B filters installed at the beamline. The collected spectra have the dark current signal subtracted to account for the systematic error and noise in the collector electronics. Subsequently, the spectra are normalized by a spectrum collected by a photodiode to account for the intensity fluctuations in the x-ray beam as a function of photon energy.

IV. EXPERIMENTAL RESULTS

In this section, we will report on the experimental details of sample deposition, experimental sample characterization and boron K-edge and phosphorus $L_{2,3}$-edge x-ray absorption spectroscopy, performed at beamline 6.3.2 at the Advanced Light Source (ALS).

A. Sample deposition

Multiple samples of $B_{12}P_2$ were grown on 4H-SiC substrates miscut 4° to the $(1\bar{1}00)$, in a cold-walled, inductively heated chemical vapor deposition (CVD) reactor. A detailed description of the deposition setup and deposition procedure under comparable conditions can be found elsewhere[26]. The substrates were placed in a TaC-coated graphite susceptor, where they were heated and etched in a H_2 carrier gas for 20 min. Sample L1 was etched at a temperature of 1650 °C and the other samples were etched at a lower temperature of 1250 °C. The carrier gas was maintained at 3500 sccm for all experiments. After the etching process was completed, the substrates were brought to the deposition temperature, which ranged from 1050 °C to 1250 °C. The B_2H_6 (1 % B_2H_6 in H_2 balance) flow rate was held constant at 40 or 60 sccm and the undiluted PH_3 was set at either 2 or 6 sccm. Given these conditions and deposition times, the expected film thicknesses are approximately of the order of 1 µm[26]. A summary of the five samples and the experimental conditions in which they were deposited is shown in Table I.

ID	B_2H_6	PH_3	H_2	p (torr)	T (°C)	t (min)
L1	80	6	3500	100	1250	15
L2	40	2	3500	100	1250	15
L3	40	2	3500	100	1150	15
L4	40	2	3500	100	1050	15
L5	40	6	3500	100	1050	15

TABLE I. Experimental conditions during deposition of the five different samples studied in this work, with partial pressures of precursor gases in sccm, total pressure p in torr, temperature T in °C and deposition time t in min.

B. X-ray absorption spectroscopy

For each of the samples listed in Table I, the x-ray absorption spectrum, at both the boron K-edge and the phosphorus $L_{2,3}$-edge, was collected in the total electron yield (TEY) mode, as shown in Fig. 1. The area under the curves has been normalized to unity to allow for meaningful comparison of relative changes in intensity of certain features. In this section we will focus the attention on the differences between the spectra collected for the different samples. Later in this article, we will provide analysis of the origin of these differences and the features themselves, using calculations from first principles.

For both edges, the spectra of samples deposited at a lower temperature are generally smoother than for samples deposited at higher temperatures; the latter have features that are more strongly defined. Typically, smoothened absorption features can be associated with distortions of the perfect crystalline lattice[11], due to thermally induced deformation of the crystalline network or localized amorphous phases. This is consistent with the notion that the likelihood of regions of the crystal growing with imperfections in the long range crystalline order, increases for decreasing deposition temperatures. The employed deposition temperatures in this work are all below 1300 K, which is currently understood to be optimal for $B_{12}P_2$ crystal growth[26].

In the phosphorus $L_{2,3}$-edge spectrum, shown in Fig. 1 (a), we highlight four features A, A', B and C that are of particular interest. Unlike in the case of K-edge transitions, due to the energy splitting of the $2p$ core level states by spin-orbit coupling, every unoccupied orbital that contributes to the overall absorption spectrum, will appear twice, separated by an energy of ΔE, which in the case of phosphorus is approximately 0.85 eV. A good example of this can be seen at feature A for sample L1, that has its corresponding spin-orbit coupled transition at feature A'. There is a strong correlation between the decrease in intensity of feature A and the decreasing deposition temperature of the sample which we will address in detail in the following sections, where we explain the origin of the feature and what structural defect

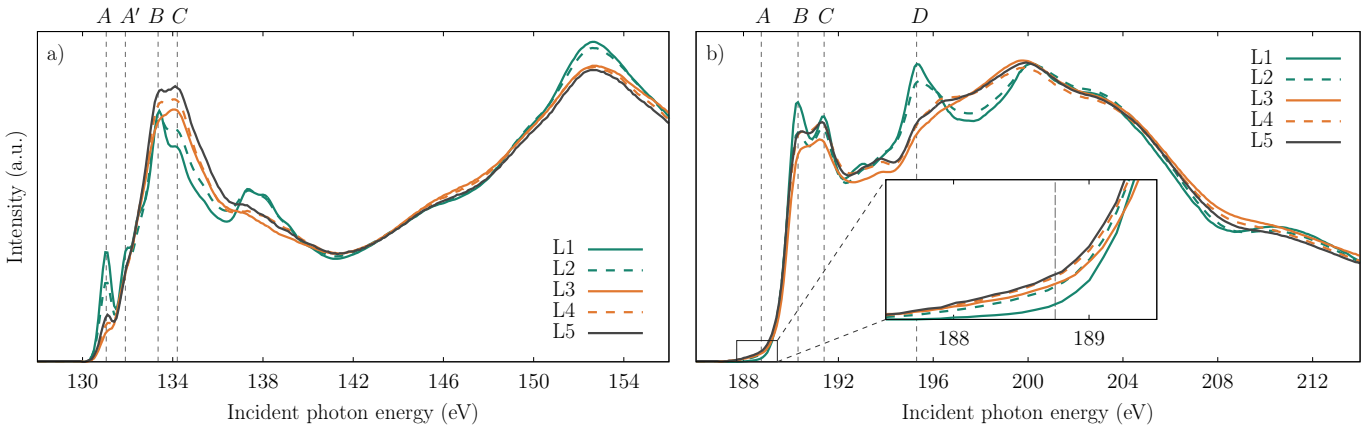

FIG. 1. (Color online) Experimentally collected x-ray absorption spectra for the (a) phosphorus $L_{2,3}$-edge and the (b) boron K-edge for five different $B_{12}P_2$ samples. The inset in panel (b) shows a close-up of the boron K-edge absorption pre-edge feature. The relative intensity is increasing for a decreasing deposition temperature of the sample.

causes its relative intensity to decrease. Features B and C are asymmetric in intensity for samples L1 and L2 but attain equal intensity for the lower temperature samples.

Turning our attention to the boron K-edge spectrum in Fig. 1 (b), we observe the same trend as for the phosphorus $L_{2,3}$-edge, where features become less well defined for samples with a lower deposition temperature. Features B and C become less well defined for samples with lower deposition temperatures and their intensity ratio changes. Samples L1 and L2 show a relatively strong transition at feature D which becomes suppressed for the other samples. All samples also showed a weak pre-edge transition, denoted as feature A, which is stronger with respect to the rest of the spectral features as the deposition temperature decreases. Similar to feature A in the phosphorus $L_{2,3}$-edge, this feature can be related to a structural defect which will be discussed in detail in later sections.

V. COMPUTATIONAL RESULTS

A. Crystal structure

A schematic representation of the crystal structure of $B_{12}P_2$ is shown Fig. 2. The fundamental building block of $B_{12}P_2$ is the boron icosahedron, which is a structural unit of 12 boron atoms that occupy the vertices of a regular icosahedron. These boron icosahedra form a rhombohedral lattice and are interconnected with dimers of phosphorus atoms, oriented parallel to the longest diagonal of the rhombohedral cell. The crystal structure has only three symmetrically unique crystal lattice sites, a phosphorus site, a boron site bound to a phosphorus atom and a boron site bound to a boron atom from a neighboring icosahedron. These different boron sites will be referred to as P-bound and B-bound boron sites and are shown in Fig. 2 (b) as black and light gray spheres, respectively.

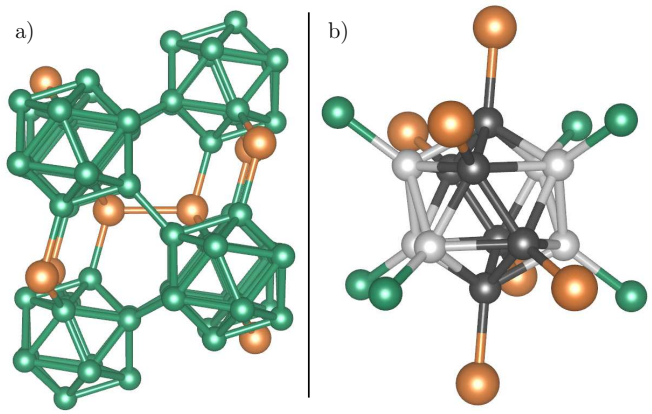

FIG. 2. (Color online) (a) A schematic depiction of the crystal structure of $B_{12}P_2$, where orange (light) spheres represent phosphorus atoms and green (darker) spheres represent boron atoms. This depiction shows six complete boron icosahedra in a rhombohedral formation with one complete phosphorus dimer positioned in the center. Panel (b) depicts a single complete icosahedron with twelve external B and P atoms it is bound to. Boron atoms bound to an external boron atom (B-bound) are indicated by a light grey sphere, whereas boron atoms bound to an external phosphorus atom (P-bound) are indicated by black spheres. Boron-boron, boron-phosphorus and phosphorus-phosphorus bonds are drawn up to a maximum of 2, 2 and 3 Å, respectively.

B. Formation energies of point defects

The three unique lattice sites in the $B_{12}P_2$ crystal structure, give a total of 6 symmetrically inequivalent antisite and vacancy defects, a boron antisite B_P, a B-bound phoshporus antisite $P_{B(B)}$, a P-bound phosphorus antisite $P_{B(P)}$, a B-bound boron vacancy $V_{B(B)}$, a P-bound vacancy $V_{B(P)}$ and a phosphorus vacancy V_P. In addition, we consider interstitial boron defects, however in stark contrast with antisite and vacancy defects, the

Defect	Boron-rich	Phosphorus-rich
B_P	2.05	4.52
$P_{B(B)}$	5.89	3.42
$P_{B(P)}$	7.16	4.69
$V_{B(B)}$	5.02	4.66
$V_{B(P)}$	5.45	5.10
V_P	4.17	6.29
I_B^A	4.84	5.20
I_B^B	5.06	5.41

TABLE II. Formation energies in eV, of boron and phosphorus, vacancies and antisites, as well as boron interstitial defects, under boron-rich and phosphorus-rich conditions. The chemical potentials for boron and phosphorus atoms were referenced with respect to the formation enthalpy of pure icosahedral boron and orthorhombic phosphorus solids.

position of interstitial defects is by definition not known *a priori*. In this work, we will use the structural definition and naming convention of two interstitial boron defects I_B^A and I_B^B, as described in another publication[1]. We have created each one of these defects in a $2 \times 2 \times 2$ $B_{12}P_2$ supercell and computed the formation energies of the relaxed defects in two limits, that represent a boron-rich and phosphorus-rich environment, as shown in Table II.

All defect structures relaxed with only minor deformations of the defective icosahedron or any of the directly neighboring icosahedra, which shows that a boron icoshedron maintains structural integrity even when in a degraded state in the presence of vacancy or interstitial defect. However, the formation energies for all of the considered defects are significant ranging between 2 eV to 7 eV, approximately. Under boron-rich conditions, the computed formation energies indicate that boron antisites and phosphorus vacancies are the most likely defects, of those considered, to be formed. When the conditions are phosphorus-rich, not surprisingly, the phosphorus vacancy has a larger formation energy, however, the boron antisite remains relatively favorable. The most likely point defect, under phosphorus rich conditions, based on these formation energies, is the phosphorus antisite at a B-bound boron crystal site. It is interesting to note that boron vacancies have relatively large formation energies in both the limits of boron- and phosphorus-richness.

C. Density of states

The density of states of the $B_{12}P_2$ crystal was calculated for both a generalized gradient approximation (PBE) and a hybrid (HSE06) exchange-correlation functional. The calculation using the PBE functional finds an indirect band gap of 2.42 eV, which compares well

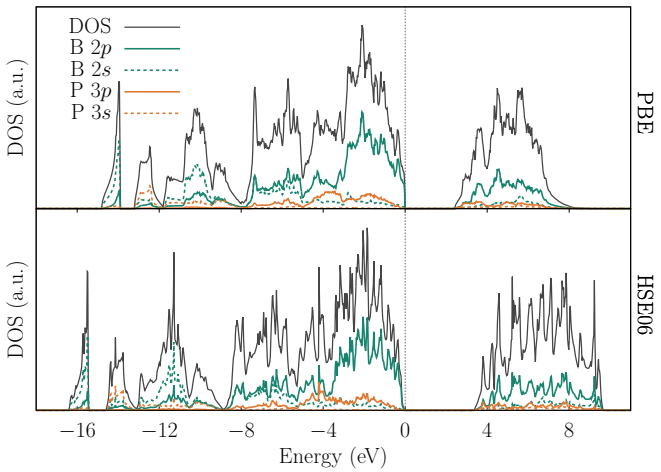

FIG. 3. (Color online) Total density of states (black solid line) and partial density of states for B $2p$ (solid green), B $2s$ (dashed green), P $3p$ (solid orange) and P $3s$ (dashed orange) orbitals computed for a PBE and HSE06 exchange-correlation functional. The energy is aligned with respect to the Fermi level, indicated by the vertical dashed line.

to other theoretical values 2.5[27], 2.63[28] and 2.79 eV[29], reported in literature. The generalized gradient approximation is infamous for underestimating the band gap, and compared to the experimental value of 3.35 eV[30], reported for $B_{12}P_2$, this is no exception. Hybrid functionals, which include a portion of exact exchange from Hartree-Fock theory in the exchange-correlation functional, are often used successfully to correct this underestimation. The density of states computed using the HSE06 functional, as shown in Fig. 3, shows a band gap of 3.39 eV, which agrees well with experiment.

Apart from the distinctive difference in energy scales and the resulting difference in the band gap, the density of states for the two different functionals agree well. The top of the valence band is dominated by states that are located on the boron atoms of the icosahedra and have a distinctive p-like character and there is almost no contribution from states on the phosphorus atoms. Contrastingly, the bottom of the conduction band comprises both B $2p$ and P $3p$ states.

D. Simulated x-ray absorption spectroscopy

In order to understand and further analyze the experimentally collected x-ray absorption spectra, we have simulated the phosphorus $L_{2,3}$-edge and boron K-edge for the perfect $B_{12}P_2$ crystal structure with the DFT-XCH method. The results are shown in Fig. 4 where the colored dashed lines represent the spectrum for the static crystal at a temperature of 0 K and the solid colored lines represent a statistical average of structural snapshots sampled from a trajectory of the perfect crystal equilibrated at 300 K. Overall the simulated spec-

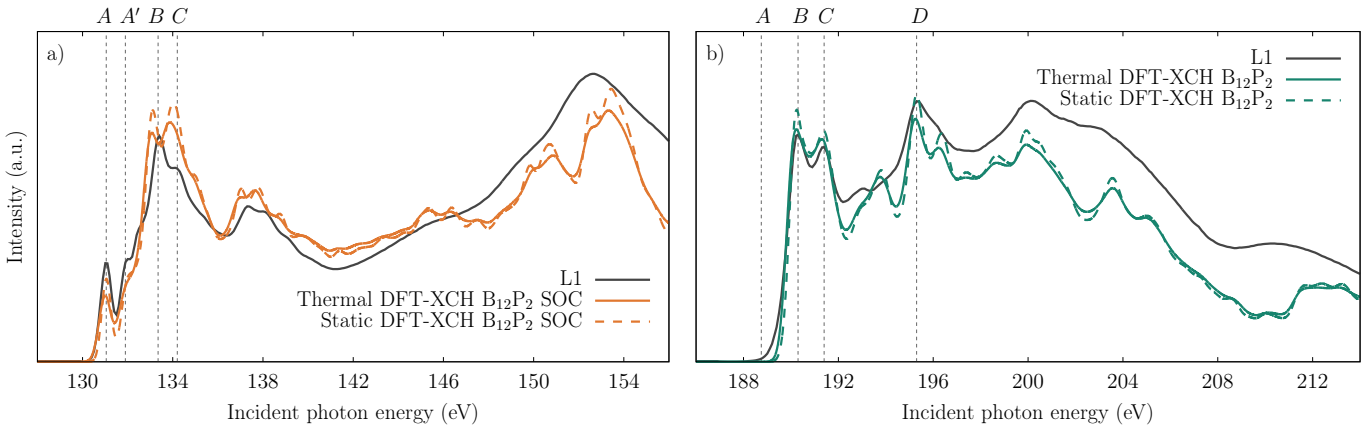

FIG. 4. (Color online) Simulated x-ray absorption spectra of the (a) phosphorus $L_{2,3}$-edge and (b) boron K-edge for the perfect $B_{12}P_2$ crystal structure at 0 K (colored dashed) and at 300 K (colored solid). For comparison, the experimental spectrum for sample L1 is plotted in both panels with a solid black line. The feature labels are identical to those in Fig. 1.

tra agree well with experiment, both for the static and thermal case. Usually, thermal distortions induced by finite temperature will smoothen the high frequency oscillations in the spectrum, as the summation of spectra from individual atoms, while they are slightly displaced from their equilibrium crystalline positions, from multiple snapshots, replicates the statistical averaging over time of the experiment[11]. In the case of $B_{12}P_2$ the effect of thermal structural distortions is minimal, with just a slight red shift of the onset of absorption for the boron K-edge.

The isolated pre-edge feature A in the P $L_{2,3}$-edge spectrum, mirrored in feature A' through spin-orbit coupling by transitions from the deeper $p_{1/2}$ core states into the same unoccupied orbital, can be attributed to an excited state with a strong σ^* character that is highly localized on the phosphorus dimer bond of the excited phosphorus atom, as visualized in Fig. 5. Feature C can be attributed to a state with negative electronic density on the phosphorus dimer, with a ring of positive electronic density concentric with the excited phosphorus atom, as displayed in Fig. 6. The outer ring of electronic density connects the three directly neighboring icosahedra that are bound to the excited phosphorus atom. The intensity of feature B originates from transitions into excited states at k-points other than the Γ point and therefore a meaningful visualization can not be made.

In the case of the B K-edge, there are two populations of symmetrically inequivalent boron atoms, B-bound and P-bound, that each have a distinct absorption spectrum. Fig. 4 shows the average of these two spectra but a deconvoluted spectrum for B-bound and P-bound boron atoms can be found Figs. 7 (a) and 7 (b), respectively. B-bound atoms predominantly contribute to features B, C and D in Fig. 4 (b). The state that gives rise to feature B is highly localized on the icosahedron containing the excited boron atom and consists of 12 lobes with distinct antibonding character. The excited state attributable to feature C, is slightly more delocalized compared to

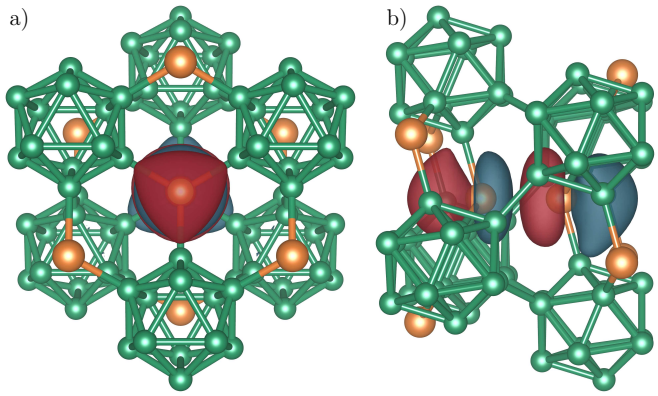

FIG. 5. (Color online) Visual representation of an isosurface of the squared wavefunction $|\psi(\vec{r})|^2$ of the state corresponding to the intense transition A at 131 eV in the P $L_{2,3}$-edge spectrum, as seen along the (a) ⟨001⟩ direction and (b) ⟨010⟩ of the crystal. The excitonic state is highly localized on the phosphorus bond and has distinct σ^* character. The two different colors of the isosurface represent the different phase of the wavefunction.

the previously described state, but remains mainly localized on the excited icosahedron. Directly on the excited boron atom, lobes with p-character are found, but the electronic density also extends along the bonds that the icosahedron forms with neighboring external atoms. Finally, the excited state giving rise to feature D has mostly π^*-like character located on the surface of the icosahedron and along the bonds it forms with its neighboring phosphorus atoms. The excited states, corresponding to the described features B, C and D, as just described, are visualized in Figs. 8, 9 and 10, with the corresponding labels S_1, S_2 and S_3 in Fig. 7 (a), respectively.

The onset of absorption from P-bound boron atoms is slightly blue shifted compared to the transitions from B-bound atoms due to the discrepancy in local electron density which is driven by the difference in electronega-

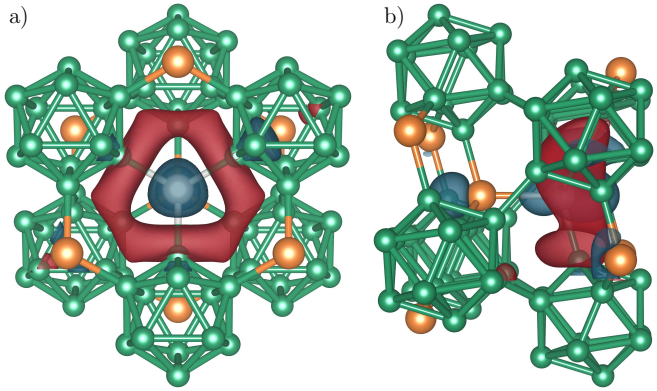

FIG. 6. (Color online) Visual representation of an isosurface of the squared wavefunction $|\psi(\vec{r})|^2$ of the state corresponding to the intense transition C at 134 eV in the P $L_{2,3}$-edge spectrum, as seen along the (a) ⟨001⟩ direction and (b) ⟨010⟩ of the crystal. The two different colors of the isosurface represent the different phase of the wavefunction.

tivity between boron and phosphorus, as can be seen in the comparison between Figs. 7 (b) and 7 (a). A boron atom bound to a phosphorus atom will effectively give up more of its electrons therefore reducing the valence screening of core excitations and increasing their binding energy. The minimum required energy to excite a core electron into the first unoccupied orbital is therefore increased, which explains the blue shift. Excitations of core electrons from P-bound boron atoms mostly contribute to features B and C, predominantly due to excitation of the core electron into two particular states. These states, labeled S_4 and S_5 in Fig. 7 (b) and visualized in Figs. 11 and 12, have similar character and localization compared to the states S_1 and S_2, respectively, which are the dominant states in the absorption spectrum of B-bound atoms. Feature A is clearly not reproduced by the simulation for the perfect crystal, which suggests that states that contribute to this part of the spectrum may be associated with states that are associated with structural defects of the crystal. We will discuss this in more detail in the following sections.

E. Defect states and spectral alignment

X-ray absorption spectra, as computed within the DFT-XCH approach, have relative energy scales and therefore, in order to allow for meaningful comparison of spectra of different systems, an energy alignment procedure, with respect to an objective reference, is required. In this work, we have adopted the approach of England *et al.*[23], which aligns the spectra with respect to the excitation energy of an isolated atom of the element of interest and the Kohn-Sham eigenvalue of the lowest energy unoccupied state into which the core-excited electron is placed. However, both the relative excitation energy, as computed from DFT total energies, and the Kohn-Sham eigenvalues include fictitious self-interaction effects. These fictitious contributions arise from the interaction of electronic orbitals with themselves as part of the effective potential of the system and become more significant for increasingly localized electronic states. Point defects often introduce defect states in the band gap of a material, which typically have a highly localized character. The point defects in $B_{12}P_2$ considered in this work are no exception and to illustrate this, the ground state density of states for the defects $P_{B(P)}$ and V_P has been plotted in Fig. 13.

Both defects clearly introduce one or multiple defect states that are located in the band gap. In the case of $P_{B(P)}$, the defect state is completely occuppied (determined by the Fermi level indicated by the dashed line), in contrast with the phosphorus vacancy V_P, which introduces multiple defect states, several of which (indicated by an arrow in Fig. 13) remain unoccupied in the ground state. When the simulated system is core-excited, the electron is placed in the first available empty state, whose Kohn-Sham eigenvalue will be used in the energy alignment scheme, including the self-interaction contribution contained within it. As long as all systems that are compared with one another, have a first available empty state with similar character and localization, the self-interaction error will be comparable and will cancel out in the relative alignment. In this situation, this is the case for $P_{B(P)}$, for which the first available empty state is the bottom of the conduction band and therefore directly comparable to the case of the pristine crystal, however, in the case of the V_P defect, the state into which the core-electron will be excited, is a defect state, which has distinct different character. As a result, the self-interaction error will also be different and the relative alignment scheme may fail.

To illustrate this, the highest occupied molecular orbital (HOMO), for the excited state of a $B_{12}P_2$ crystal containing either a $P_{B(P)}$ or V_P defect and a reference atom far away from the structural defect in its core-excited state, is visualized in Figs. 14 (a) and 14 (b), respectively. The isosurface values were chosen such that an equal amount of the total charge density is contained within the respective surfaces and the isosurface representation of the HOMO in the bulk system shown in Fig. 5. This enables a direct comparison of the locality of the excited states. The HOMO of the core-hole excited system containing the $P_{B(P)}$ defect has a strong σ^* character and strongly resembles the HOMO of the core-excited perfect crystal [see Fig. 5 (b)] and both states are comparably localized, as predicted by the calculated density of states. However, contrastingly, the HOMO for the V_P containing system, which corresponds to the empty state in the ground state density of states marked by the arrow in Fig. 13 (b), clearly has a more localized character, in this case due to the missing phosphorus atom. Due to the increased locality of this HOMO compared to the HOMO in the bulk system, the self-interaction energy error will increase and when using the same ab-

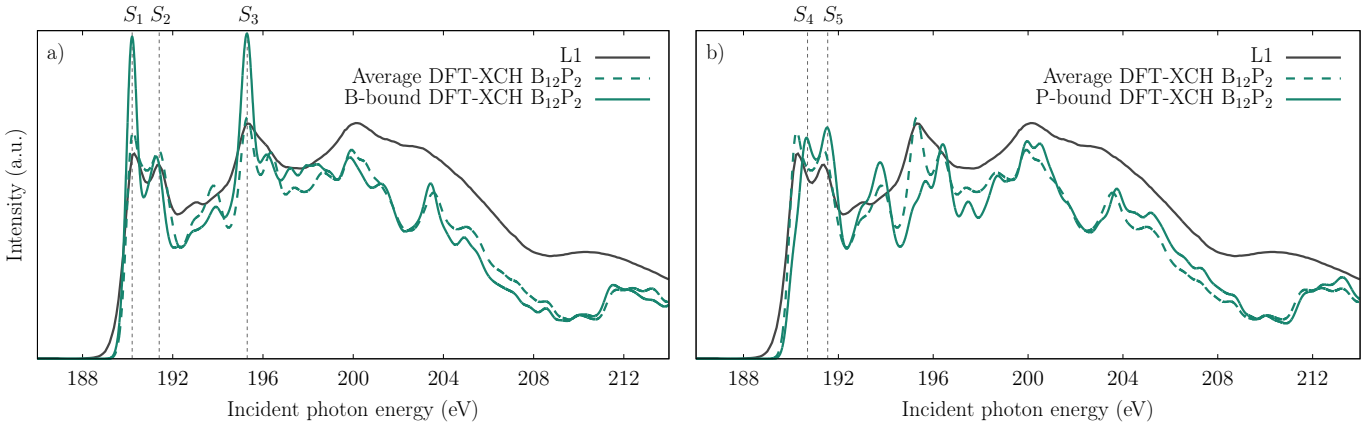

FIG. 7. (Color online) Deconvoluted average computed B K-edge for the static $B_{12}P_2$ crystal cell for (a) B-bound and (b) P-bound boron atoms. The solid green line represents the respective partial spectrum and the dashed green line is the average of the B-bound and P-bound spectrum, which corresponds directly to the dashed green line shown in Fig. 4 (b). The solid black line corresponds to the experimental spectrum collected for sample L1. The vertical dashed lines indicate the positions of states that are most intense and dominate the shape of the partial spectra. Visual representations of the electronic density of these states, are displayed in Figs. 8 to 12, corresponding to the labels S_1 to S_5, respectively.

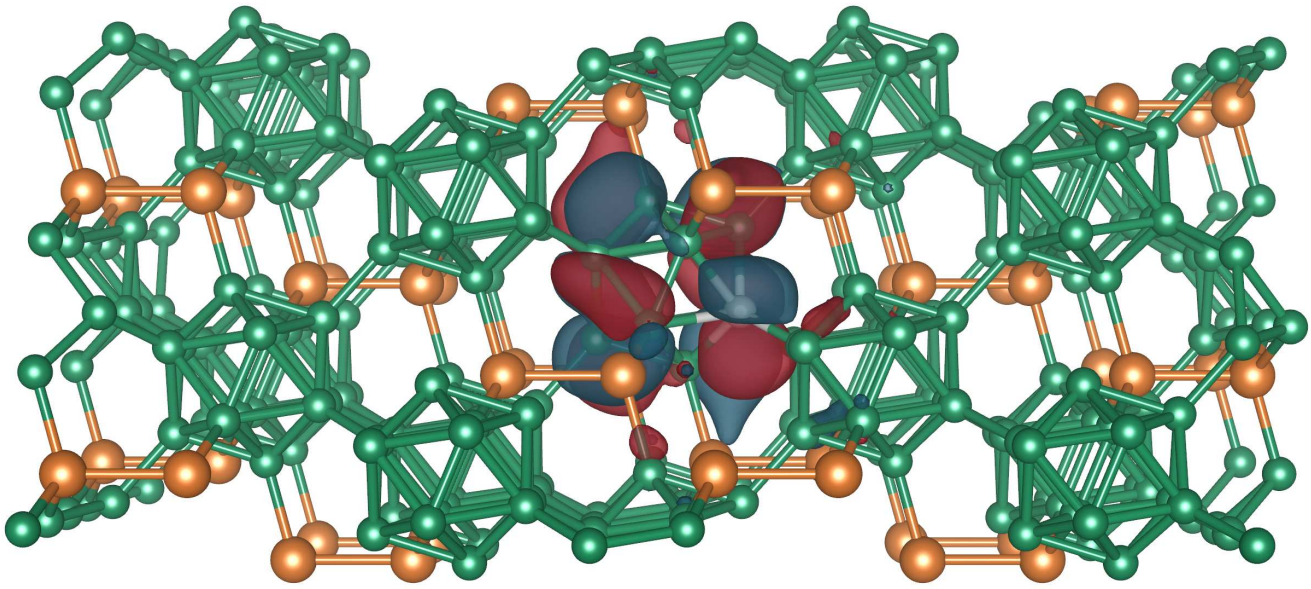

FIG. 8. (Color online) Visual representation of an isosurface of the squared wavefunction $|\psi(\vec{r})|^2$ of the state corresponding to the intense transition S_1 in the B K-edge spectrum of B-bound atoms [see Fig. 7 (a)], as seen along the $\langle 010 \rangle$ of the crystal. The excited boron atom is shown in gray and the two different colors of the isosurface represent the different phase of the wavefunction.

solute alignment energy for both systems, the spectrum of the defective system will be red-shifted compared to experiment.

This can be seen in Figs. 15 (a) and 15 (b), which shows the computed x-ray absorption spectra for the $P_{B(P)}$ and V_P containing system. The black solid line represents the measured spectrum for sample L1, whereas the solid orange line corresponds to the computed average spectrum for all atoms within a radius of 3.3 Å of the structural defect and the dashed orange line is the computed spectrum for the distant reference atom, whose first excited state was visualized in Fig. 14 (b). For the $P_{B(P)}$ defect, the σ^* feature aligns perfectly with experiment, as the self-interaction error is comparable to that of the bulk calculation for which the initial alignment was done, however for the phosphorus vacancy, there is a significant mismatch of almost 0.5 eV. Note that the mismatch is also present for the spectrum of the reference atom, far removed from the defect. In this particular case, the mismatch for the average and reference atom spectrum are

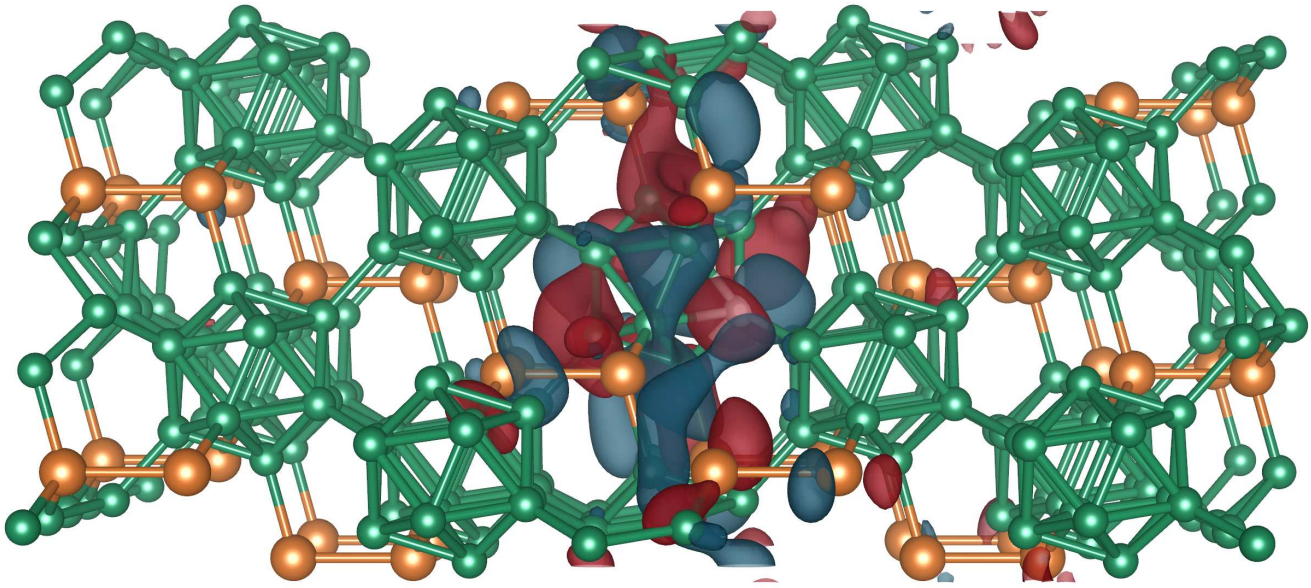

FIG. 9. (Color online) Visual representation of an isosurface of the squared wavefunction $|\psi(\vec{r})|^2$ of the state corresponding to the intense transition S_2 in the B K-edge spectrum of B-bound atoms [see Fig. 7 (a)], as seen along the $\langle 010 \rangle$ of the crystal. The excited boron atom is shown in gray and the two different colors of the isosurface represent the different phase of the wavefunction.

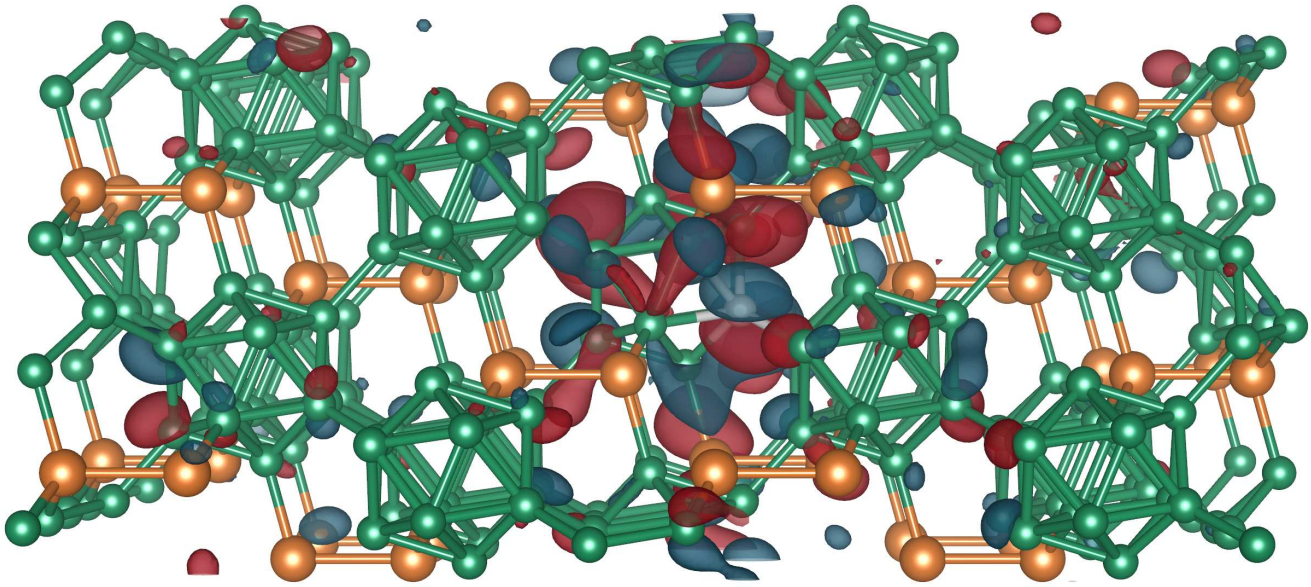

FIG. 10. (Color online) Visual representation of an isosurface of the squared wavefunction $|\psi(\vec{r})|^2$ of the state corresponding to the intense transition S_3 in the B K-edge spectrum of B-bound atoms [see Fig. 7 (a)], as seen along the $\langle 010 \rangle$ of the crystal. The excited boron atom is shown in gray and the two different colors of the isosurface represent the different phase of the wavefunction.

identical, but this is not necessarily always the case and therefore correcting the self-interaction alignment error by aligning with respect to the reference atom, is not an option. A robust scheme to correct for the self-interaction error in the current energy alignment scheme is not available. In this work, this problem is overcome by directly aligning the individual atomic spectra of a specific structural configuration with respect to the position of the σ^* feature, relative to the same feature in the computed spectrum for the bulk material.

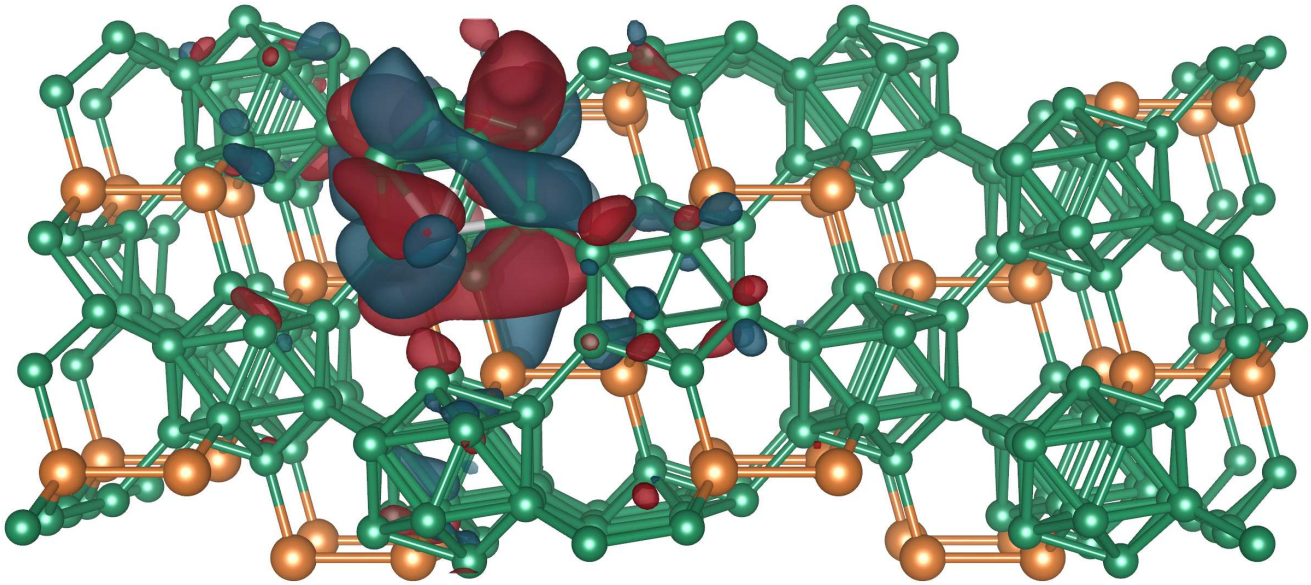

FIG. 11. (Color online) Visual representation of an isosurface of the squared wavefunction $|\psi(\vec{r})|^2$ of the state corresponding to the intense transition S_4 in the B K-edge spectrum of P-bound atoms [see Fig. 7 (b)], as seen along the $\langle 010 \rangle$ of the crystal. The excited boron atom is shown in gray and the two different colors of the isosurface represent the different phase of the wavefunction.

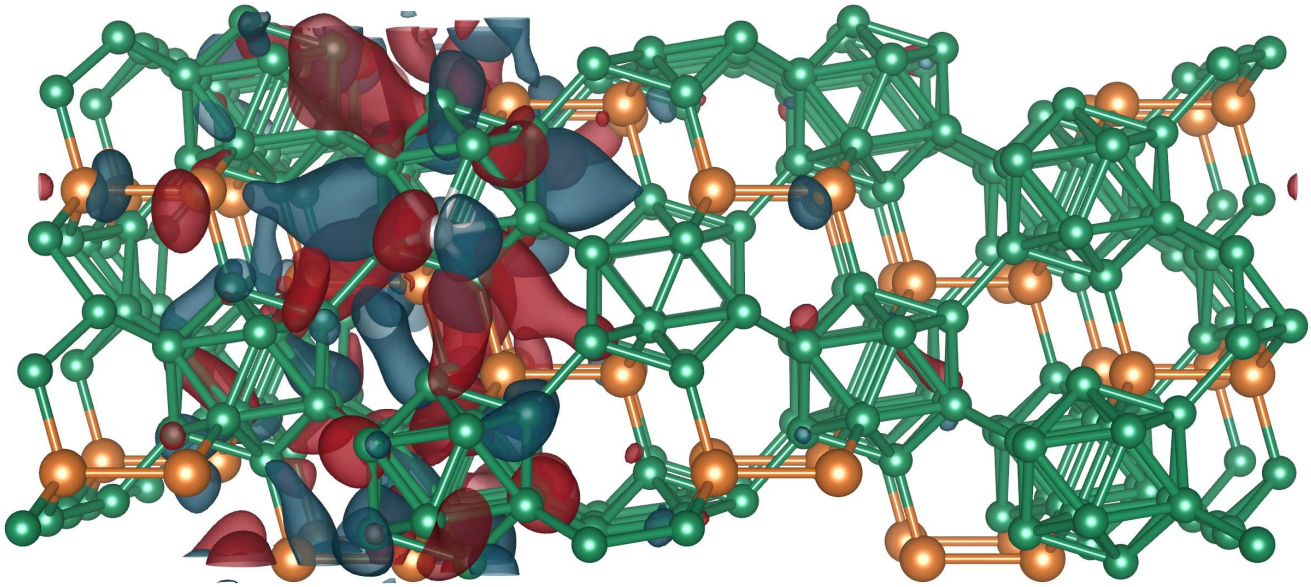

FIG. 12. (Color online) Visual representation of an isosurface of the squared wavefunction $|\psi(\vec{r})|^2$ of the state corresponding to the intense transition S_5 in the B K-edge spectrum of P-bound atoms [see Fig. 7 (b)], as seen along the $\langle 010 \rangle$ of the crystal. The excited boron atom is shown in gray and the two different colors of the isosurface represent the different phase of the wavefunction.

F. Point defect x-ray absorption spectroscopy

To investigate the influence of structural point defects of the crystalline structure on the x-ray absorption spectrum of $B_{12}P_2$, and whether they can explain the differences in the experimental spectra and reproduce features that are not predicted for the perfect crystal lattice, we consider vacancy, interstitial and antisite defects. We have computed the average x-ray absorption spectrum of boron and phosphorus atoms that are within a radius of 3.4 and 4.0 Å, respectively, of the point defect. Either the appearance of new features or the reduction of features

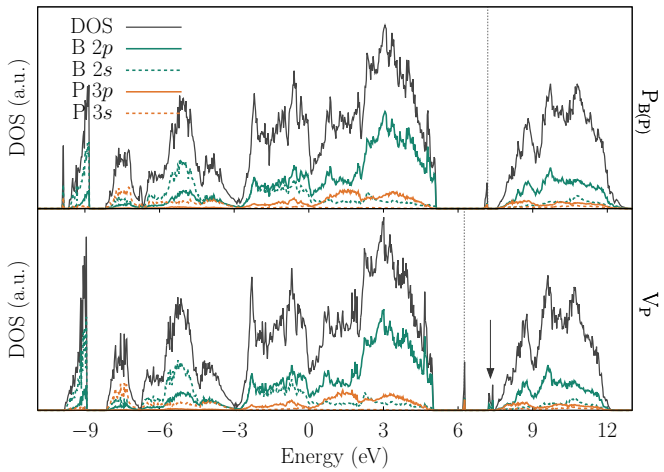

FIG. 13. (Color online) Ground state total density of states (black solid line) and partial density of states for B $2p$ (solid green), B $2s$ (dashed green), P $3p$ (solid orange) and P $3s$ (dashed orange) orbitals computed for the $B_{12}P_2$ supercell containing a (top) $P_{B(P)}$ or (bottom) V_P defect. The Fermi level is indicated by a vertical dashed line. Defect states that are unoccupied in the ground state for the V_P defect, are indicated by the black arrow.

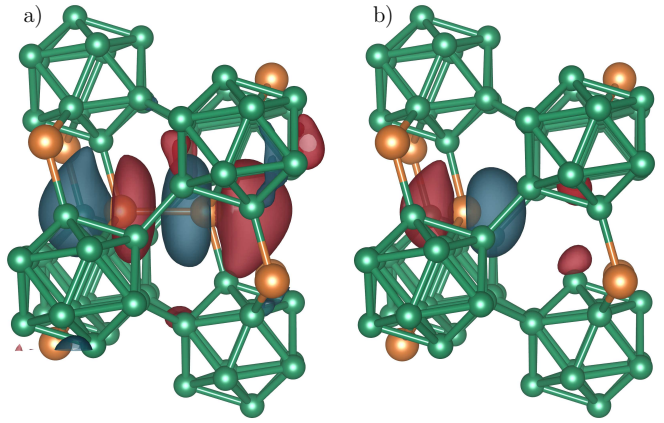

FIG. 14. (Color online) Visual representation of an isosurface of the squared wavefunction $|\psi(\vec{r})|^2$ of the highest occupied electronic states in the excited state of a system containing a (a) $P_{B(P)}$ or (b) V_P defect. The core-hole excited atom is approximately 10 Å removed from the structural defect and the excited state is localized on the excited boron atom in the case of the $P_{B(P)}$ defect. This is however not necessarily the case, as clearly, for the V_P defect, the excited state is not localized on the excited atom, but rather on the V_P defect itself.

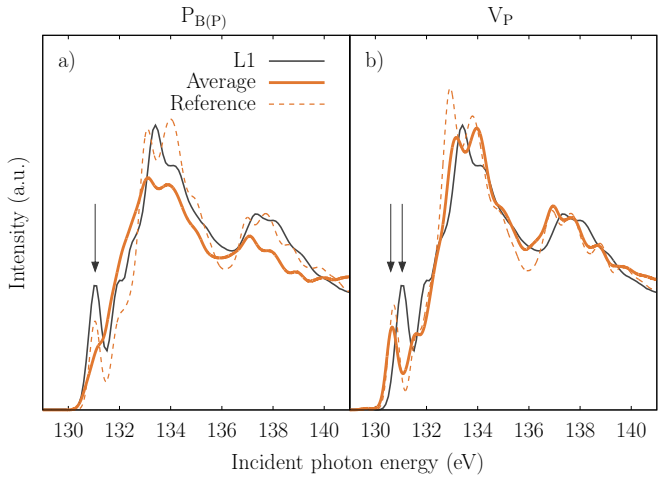

FIG. 15. (Color online) Experimental P $L_{2,3}$ spectrum of sample L1 (solid black line) and the computed spectra (orange lines) for a $B_{12}P_2$ supercell containing a $P_{B(P)}$ or V_P defect, in the left and right panel, respectively. The solid orange lines represent the average spectrum of all the atoms in the direct vicinity of the defect, whereas the dashed orange line is the computed spectrum of a reference atom far removed from the structural defect. The vertical black arrows indicate the locations of the σ^* transitions for both the experimental and simulated spectra.

that were present in the crystalline spectrum, can provide evidence for which point defects are present in the experimental samples. These changes are most apparent at the onset of the absorption spectrum and therefore Fig. 16 shows the onset of the computed x-ray absorption spectra for the eight different point defects listed in Table II, for both the boron K-edge and phosphorus $L_{2,3}$-edge.

A perfect example of defects that introduce new spectral features, are boron vacancies, which open defect states within the band gap and as boron atoms, that are directly adjacent to the vacancy, are core excited into these defect states, a strong absorption feature appears below the main absorption edge of the B K-edge spectrum. For both types of boron vacancies, this defect feature is predicted to appear at an energy of 187 eV, which is far below the energy of the main absorption edge found in experiment. Even though this result suggests a lack of boron vacancies in the experimental samples, this does not guarantee a complete absence of boron vacancies, as the chance of detecting the defect feature depends on both the intensity resolution of the experimental setup, as well as the oscillator strength of the specific defect state and the relative abundance of vacancies present in the sample. Our simulations predict an oscillator strength for boron vacancy defect states that is approximately half the intensity of the most intense feature in the B K-edge for an unperturbed boron atom in a perfect crystal environment. With an experimental intensity resolution on the approximate order of 1×10^{-2} and the fact that for every boron vacancy, five adjacent boron atoms will contribute to these defects states, we expect to be able to resolve a defect concentration of the order of 1×10^{-3} to 1×10^{-2}. Following the same argumentation as for boron vacancies, the presence of B_P and I_B^A defects in the samples is also found to be unlikely, since these defects also introduce defect transitions in the x-ray absorption

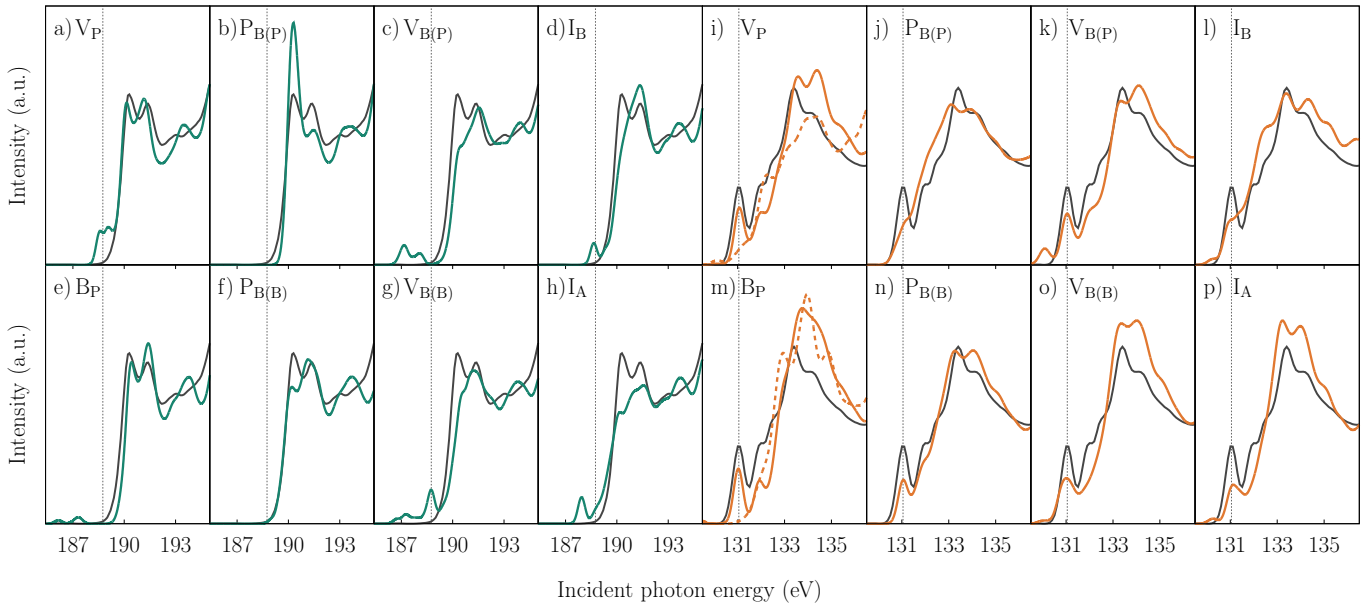

FIG. 16. (Color online) Computed x-ray absorption spectra for vacancy, interstitial and antisite defects for the (a-h) B K-edge and (i-p) P $L_{2,3}$-edge. The solid black lines represents the experimentally collected spectrum for samples L1 and the colored solid lines are the computed spectra. The computed spectra are the average of the boron and phosphorus atoms within a radius of 3.4 and 4.0 Å, respectively, of the point defect. The labels in the top left corner of the images indicate the type of the defect and correspond to the structures and formation energies in Table II. Colored dashed lines, when present, indicate the spectrum of an atom directly neighboring or at the position of the defect. The vertical dashed lines indicate the position of features A in both the B K and P $L_{2,3}$ spectra, in correspondence with the labels used in Figs. 1 and 4

spectra at energies where the experimental absorption is negligible.

The V_P, $P_{B(B)}$ and I_B^B defects also introduce defect states when neighboring boron atoms are core excited, however, in contrast with the previously discussed defects, these defect states appear at higher energies in the spectrum and overlap exactly with feature A in the B K-edge, marked by the dotted line in Fig. 16 (a)-(h). Feature A can therefore be associated with any one of these defects and the fact that feature A becomes relatively more intense for samples that were deposited at lower temperatures, for which one expects more structural defects, is in good agreement with this prediction. Additionally, the low formation energies for V_P and $P_{B(B)}$ defects (see Table II), show these are the most probable defects under boron and phosphorus-rich conditions, respectively.

Up until now, we determined the presence of point defects by verifying the presence of their characteristic defect transitions that would be absent in the spectrum of the perfect crystal. Analogously, it is also possible to observe the presence of certain defects by studying the suppression of spectral features observed in the spectrum of the perfect crystal, prime examples of which, are the boron antisite and phosphorus vacancy. The intensity of the characteristic feature A observed in the phosphorus $L_{2,3}$-edge for the bulk, is significantly reduced or completely suppressed for both the B_P and the V_P defect. Note that this effect is not directly apparent in the average spectrum, represented by the solid line in Figs. 16 (i) and 16 (m), however the spectrum of the atom directly neighboring the point defect, indicated by the dashed line in the same figures, clearly shows the almost full suppression of feature A. Upon closer inspection, this is not suprising at all, since that absorption feature is due to a highly localized σ^* state on the P_2 dimer, as shown in Fig. 5, and both the B_P and V_P defect effectively destroy the phosphorus dimer and thereby the bond. The relatively decreasing intensity of feature A as observed in experiment for the samples deposited at lower temperatures can therefore be directly linked to presence of boron antisite or phosphorus vacancy defects.

Based on observations made from the B K-edge point defect spectroscopy, it can be concluded that the defects V_P, I_B^B and $P_{B(B)}$, are potentially present in the samples studied in this work. Analysis of the P $L_{2,3}$ edge spectroscopy shows that both V_P and B_P defects can explain the gradual decrease of feature A observed in the experimental samples deposited at lower temperatures. The fact that the presence of phosphorus vacancies is supported independently by the spectroscopy of both absorption edges and that the formation energy of the defect is computed to be the lowest, after the B_P formation energy, for all considered defects in boron-rich conditions, is evidence that the analyzed samples contain a significant amount of phosphorus vacancies. Determining exact defect quantities is difficult, but the relative difference in the intensity of the σ^* feature in the P $L_{2,3}$-edge of the

studied samples and the increasing intensity of feature A in the B K-edge, would place a careful estimation of phosphorus vacancy abundances on the order of 1 % for the samples deposited at the lower temperatures.

The ability to quantify defect levels with XANES is limited by both the relative intensity of defect states with respect to the spectrum of the bulk, as well as the intensity sensitivity of the experimental setup. The defects discussed in this work typically have associated defect transitions with intensities that are of the same order as bulk transitions and the relative intensity resolution of the experiment is on the approximate order of 1×10^{-3} to 1×10^{-2}. This means that XANES is not a suitable technique to estimate, for example, doping concentrations, which typically have concentrations that are far more dilute. However, our results have clearly shown that x-ray absorption spectroscopy is sensitive to different types of defect populations with a relative concentration of the order of 1×10^{-3} or higher, and that relative changes in their abundances can be qualitatively assessed. This technique can therefore prove to be valuable in monitoring defect populations in applications where the relevant material properties are affected negatively by the presence of a significant amount of structural defects.

VI. CONCLUSIONS

We have presented the experimentally collected x-ray absorption spectroscopy of the B K and P $L_{2,3}$ edge for several $B_{12}P_2$ samples, grown in a chemical vapor deposition reactor under varying experimental conditions. Simulated x-ray absorption spectra from first-principles, for the perfect crystal at zero and finite temperature, showed great agreement with experiment and facilitated the analysis of spectral features and tracing their origin in the electronic structure of the material. We have discussed point defects as the potential cause for the remaining discrepancies between simulated x-ray absorption spectra for the perfect crystal and the experimental data, as well as the source of the relative difference observed in the spectra for the different samples that were analyzed. To this end, we have simulated the spectroscopic signature of antisite, interstitial and vacancy point defects in both the B K and P $L_{2,3}$ edge. The results showed that the relatively increasing intensity of the pre-edge feature in the B K-edge and the relatively decreasing intensity of the first feature in the P $L_{2,3}$ edge, for samples deposited at decreasing temperatures, both can be explained by the presence of phosphorus vacancies in the samples. Combined with the fact that the computed formation energy of phosphorus vacancies is among the lowest of all the considered defects under boron-rich conditions, it is likely that this is the type of defect that is most abundant in the analyzed samples.

Contrastingly, simulations of the x-ray absorption spectroscopy of boron vacancies predict strong absorption features below the main onset of absorption in the B K-edge spectrum, due to the introduction of defect states in the band gap by the defect, which leads to the conclusion that the experimental samples contain little to no boron vacancies. The observed lack or absence of boron vacancies, is reminiscent of the "self-healing" property of icosahedral borides like $B_{12}P_2$, that has been reported in literature[4,6]. Transmission electron microscopy measurements of $B_{12}P_2$ showed virtually no evidence of amorphization or crystal structure damage, despite having been subjected to intense and highly energetic particle beams. The suggested cause for the observed lack of damage, was the spontaneous recombination of defects, created by the displacement of boron atoms. Recent theoretical work has shown that the activation energies for the recombination of boron vacancies with interstitial boron atoms can be so low that recombination will be spontaneous[1]. This is in strong agreement with the spectroscopic analysis discussed in this work which also finds strong evidence for the lack of boron vacancies. The simulated spectroscopic signatures of point defects, presented in this work, can be used in future studies of the dynamics of defect creation and recombination in $B_{12}P_2$.

ACKNOWLEDGMENTS

This work is supported by NanoNextNL, a micro and nanotechnology programme of the Dutch Government and 130 partners. We acknowledge the support of the Center for X-ray Optics of Lawrence Berkeley Laboratory and the Industrial Focus Group XUV Optics at the MESA+ Institute for Nanotechnology at the University of Twente, notably the partners ASML, Carl Zeiss SMT GmbH, and the Foundation FOM. All the computational work was performed at the Molecular Foundry which is supported by the Office of Science, Office of Basic Energy Sciences, of the United States Department of Energy under Contract No. DE-AC02-05CH11231.

* shuber@lbl.gov

[1] S. P. Huber, E. Gullikson, C. D. Frye, J. H. Edgar, R. W. E. van de Kruijs, F. Bijkerk, and D. Prendergast, Chemistry of Materials **28**, 8415 (2016).

[2] Q. An and W. A. Goddard, Chemistry of Materials **27**, 2855 (2015).

[3] J. C. Lund, F. Olschner, F. Ahmed, and K. S. Shah, MRS Proc. **162**, 601 (1989).

[4] D. Emin, Journal of Solid State Chemistry **179**, 2791 (2006).

[5] T. P. Viles, B. A. Brunett, H. Yoon, J. C. Lund, H. Hermon, D. Buchenauer, K. McCarty, M. Clifft, D. Dibble, and R. B. James, MRS Proc. **487**, 585 (1997).

[6] M. Carrard, D. Emin, and L. Zuppiroli, Phys. Rev. B **51**, 11270 (1995).
[7] I. Jiménez, A. F. Jankowski, L. J. Terminello, D. G. J. Sutherland, J. A. Carlisle, G. L. Doll, W. M. Tong, D. K. Shuh, and F. J. Himpsel, Phys. Rev. B **55**, 12025 (1997).
[8] M. Niibe, K. Miyamoto, T. Mitamura, and K. Mochiji, Journal of Vacuum Science & Technology A **28**, 1157 (2010).
[9] I. Caretti and I. Jiménez, Journal of Applied Physics **110**, 023511 (2011).
[10] K. Simonov, N. Vinogradov, M. Ng, A. Vinogradov, N. Mårtensson, and A. Preobrajenski, Surface Science **606**, 564 (2012).
[11] S. P. Huber, E. Gullikson, R. W. E. van de Kruijs, F. Bijkerk, and D. Prendergast, Phys. Rev. B **92**, 245310 (2015).
[12] G. Kresse and J. Furthmüller, Physical Review B **54**, 11169 (1996).
[13] P. E. Blöchl, Physical Review B **50**, 17953 (1994).
[14] G. Kresse and D. Joubert, Physical Review B **59**, 1758 (1999).
[15] J. P. Perdew, K. Burke, and M. Ernzerhof, Phys. Rev. Lett. **77**, 3865 (1996).
[16] H. J. Monkhorst and J. D. Pack, Phys. Rev. B **13**, 5188 (1976).
[17] P. E. Blöchl, O. Jepsen, and O. K. Andersen, Phys. Rev. B **49**, 16223 (1994).
[18] A. V. Krukau, O. A. Vydrov, A. F. Izmaylov, and G. E. Scuseria, The Journal of Chemical Physics **125**, 224106 (2006).
[19] H.-P. Komsa, T. T. Rantala, and A. Pasquarello, Physical Review B **86**, 045112 (2012).
[20] C. G. V. de Walle, J. Appl. Phys. **95**, 3851 (2004).
[21] D. Prendergast and G. Galli, Phys. Rev. Lett. **96**, 215502 (2006).
[22] E. L. Shirley, Physical Review B **54**, 16464 (1996).
[23] A. H. England, A. M. Duffin, C. P. Schwartz, J. S. Uejio, D. Prendergast, and R. J. Saykally, Chemical Physics Letters **514**, 187 (2011).
[24] J. Underwood and E. Gullikson, Journal of Electron Spectroscopy and Related Phenomena **92**, 265 (1998).
[25] E. M. Gullikson, S. Mrowka, and B. B. Kaufmann, "Recent developments in euv reflectometry at the advanced light source," (2001).
[26] C. Frye, C. Saw, B. Padavala, R. Nikolić, and J. Edgar, Journal of Crystal Growth **459**, 112 (2017).
[27] D. R. Armstrong, J. Bolland, and P. G. Perkins, Theoretica Chimica Acta **64**, 501 (1984).
[28] D. Li and W. Y. Ching, Phys. Rev. B **52**, 17073 (1995).
[29] W. Hayami and S. Otani, J. Phys. Chem. C **112**, 2711 (2008).
[30] G. A. Slack, T. McNelly, and E. Taft, Journal of Physics and Chemistry of Solids **44**, 1009 (1983).